Field statistics of two vectorially superposed wave populations

Iver H. Cairns, P. A. Robinson, and P. Das
School of Physics, University of Sydney, New South Wales 2006, Australia
(Received 16 May 2002; revised manuscript received 3 September 2002; published 30 December 2002)

Field statistics of observed waves and radiation constrain the physics of the emission process and source region. However, data often contain two or more superposed signals or a signal superposed on a noise background, creating difficulties for interpretation. Here, the combined probability distribution of the field formed by vector superposition of two signals, each with specified statistics, is written as a double integral with integrable singularities. The analytic result and its numerical solutions for combinations of Gaussian and lognormally distributed signals show that these predictions differ from those for field or intensity convolution and from the individual wave distributions. At high fields, the combined distribution takes the qualitative form of the dominant individual distribution (which is localized or otherwise extends to larger fields) but develops a significant tail at low fields due to vector superposition of almost antiparallel fields with similar magnitudes. It is shown that very nearly power-law distributions can develop in significant field domains, despite neither component distribution being power law. This is relevant to alternative interpretations in terms of self-organized criticality and certain modulational wave instabilities. The formalism is then applied to observations of the Vela pulsar, resulting in greatly improved fits to data and different interpretations. Specifically, the results are strong evidence that stochastic growth theory (SGT) is relevant and that the approximate power-law statistics found at some phases are not intrinsic but rather due to vector convolution of a Gaussian background with a lognormal; the latter is interpretable in terms of SGT. The field statistics are consistent with the emission mechanism being a direct linear instability or indirect generation via linear mode conversion of nonescaping waves driven by a linear instability. They are inconsistent with nonlinear self-focusing instabilities generating the observed pulsar radiation. This formalism and its results should also be widely applicable to other types of wave growth in inhomogeneous media.

DOI: 10.1103/PhysRevE.66.066614 PACS number(s): 46.65.+g, 02.50.−r, 95.30.−k, 95.75.−z

I. INTRODUCTION

The field statistics of plasma waves and radiation are emerging research areas of space physics, astrophysics, and plasma physics. In contrast, Fourier, correlation, and other studies of an emission's temporal and frequency properties are both conventional and long studied. Correlation analyses, for instance, are standard because they reveal dispersive and scintillation effects due to scattering in and propagation through inhomogeneous plasmas [1]. Emphasis on field statistics is relatively new, however, and has followed from the study of wave growth in inhomogeneous plasmas.

Characterizing the bursting of observed signals in terms of field statistics is worthy in its own right as an analysis tool, but its importance for developing physics-based theories for natural phenomena is considerably stronger. Particularly for remote observations, such as space and astrophysical sources where *in situ* observations are not possible, analyses of field statistics potentially open a new window into the source physics. As summarized in detail below, the reason is that the field statistics depend on the emission mechanism(s) for the waves, the physics of the wave-particle-background plasma system in the source (and so on the source plasma parameters), scattering/propagation effects between the source and observer, and whether one or more processes in a single source, or in multiple sources, contribute to the observed variability. Put in another way, theory-data comparisons allow the active emission mechanism(s) and source physics to be constrained by, and ideally inferred from, the observed field statistics. This paper presents theory related to disentangling the number of active processes and/or sources contributing to observed field statistics, application of this theory to the Vela pulsar, and discussion of the resulting implications for the emission mechanism and source physics responsible for pulsar radio emissions.

A number of theoretical predictions now exist for the field statistics of waves or radiation, each dependent on the emission mechanism, source physics, and/or scattering/propagation effects. First, the usual model for wave growth in plasmas [2–4], involving spatially uniform secular amplification at a constant rate until limited by nonlinear effects, predicts that the probability distribution of wave electric fields E, $P(E)$, should be uniformly distributed in $\log E$ ($\equiv \log_{10} E$ here) below the nonlinear threshold. Second, radiation from a large number of incoherently superposed sources, or scattering by density irregularities [1], should produce Gaussian intensity distributions, where the intensity $I \propto E^2$. Third, self-organized criticality (SOC) [5,6], which describes the self-consistent evolution of a waves-particles-plasma background system near marginal stability, should produce a power-law distribution for energy releases with index close to -1 (but ranging from ≈ -0.5 to -2). Fourth, pure stochastic growth theory (SGT), which describes the evolution of a self-consistent wave-particle system driven stochastically near marginal stability in a prescribed inhomogeneous plasma background, predicts lognormal statistics [7–11]. (Note that most natural plasmas are expected to evolve to states close to marginal stability, where emission and absorption are closely balanced, due to

operation of plasma instabilities and the large distances and times available for relaxation.) Fifth, the combination of SGT with nonlinear processes alters the field statistics primarily near and above the lowest threshold field E_c for the nonlinear processes; if a nonlinear three-wave process removes energy from the waves then the lognormal distribution exhibits a nonlinear cutoff near E_c with known analytic form, while nonlinear self-focusing processes such as modulational instability and wave collapse cause a power-law tail to develop above E_c with $P(E) \propto E^{-\alpha}$ and α ranging from 3 to 7 [11–13], depending on the dimensionality, shape (isotropic versus oblate versus prolate), and subsonic/supersonic character of the collapsing wave packets. Sixth, waves driven stochastically from thermal levels by an instability, but sufficiently weak to retain memory of their thermal past, can also develop a power-law tail [14,15]. Finally, the elementary burst theory (EBT) [16,17] involves systems in which waves and particles interact self-consistently in growth sites but do not evolve to a SGT state. The EBT systems have exponential statistics.

SOC applies widely to bursty phenomena active over a wide range of spatial, temporal, or energy scales [5], with applications including earthquakes [18], condensed matter physics [19], solar flares [20], auroral physics, and perhaps pulsars [21]. The Jovian "*S*" bursts also show a power-law flux distribution [22], for which SOC or driven thermal waves [14,15] may be relevant. SGT is also attractive due to its ability to explain the bursting and variability of natural emissions in systems near marginal stability, with widespread applicability to space and astrophysical phenomena. It applies to all eight phenomena analyzed by us to date: Langmuir waves in interplanetary type-III solar radio sources [8], Langmuir waves in the main volume of Earth's foreshock [9,10,23], thermal and driven thermal Langmuir waves in the solar wind and edge of Earth's foreshock, respectively [15], mirror mode and electromagnetic ion cyclotron waves in Earth's magnetosheath [24], waves near the electron plasma frequency f_p over Earth's polar cap [25], and radio emissions from the Vela pulsar [26]. In contrast, EBT apparently applies to solar decimetric spike bursts [17,27] but the uniform secular growth model is inconsistent with the field statistics measured in all these applications.

Often observed signals consist of the superposition of a signal of interest and a noise background or the superposition of two or more signals of interest, the latter corresponding to either multiple emission mechanisms in a single source or multiple subsources along the same line of sight. How are the field statistics affected by these superpositions? Here, this question is investigated analytically and numerically for transverse (two-dimensional) electromagnetic signals, with specific attention to observations of the Vela pulsar [26,28,29]. Related applications exist for the superposition of Langmuir waves and electromagnetic radiation near f_p in the solar wind and Earth's foreshock [15] and the superposition of electrostatic waves near f_p with whistler-mode hiss over Earth's polar cap [25].

It is shown in Sec. II that the combined probability distribution, formed by vector combination of two fields $\mathbf{E}_1$ and $\mathbf{E}_2$ described by separate probability distributions, is given by an integral with integrable singularities. This integral shows that the combined field statistics are generally different from the statistics obtained by direct convolution of either the intensity distributions or the field distributions because a vector field convolution is required. In Sec. III, the combined field statistics are investigated numerically for both Gaussian and lognormal distributions, showing that they are, in general, different from those of the individual distributions or the results for intensity or amplitude convolution. It is shown that at high fields, the combined distribution is close to the dominant individual distribution but develops a significant tail at low fields. The origin of this tail and the development of approximate power-law regions at high fields are described and explained. These effects are illustrated in Sec. IV using data for the Vela pulsar [26,28,29]. The use of the two-component analysis leads to significantly improved fitting of the data and changes in their physical interpretation. The implications of the Vela results for understanding pulsar emissions are discussed in Sec. V, together with suggestions for other applications. The paper's conclusions are summarized in Sec. VI.

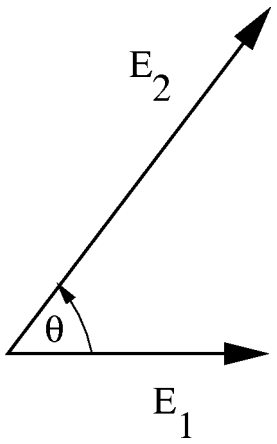

FIG. 1. Fields $\mathbf{E}_1$ and $\mathbf{E}_2$ have magnitudes E_1 and E_2 and an angle θ between them.

Although the foregoing Introduction is focused primarily on wave growth in plasmas (especially space and astrophysical plasmas), the problem addressed and theoretical results obtained should be of more general interest. As well as being relevant to laboratory plasma physics, space physics, and astrophysics, they apply equally to wave growth in other inhomogeneous media.

II. ANALYTICS

The observed field $\mathbf{E}$ is formed by vector addition of two fields $\mathbf{E}_1$ and $\mathbf{E}_2$ that are transverse to the measurement plane (Fig. 1), described by their magnitudes E_1 and E_2, and the angle θ between them. The probability distribution $P(E^2)$, written as a function of E^2 and normalized by $\int_0^\infty d(E^2)P(E^2)=1$, is defined by

$$P(E^2)=2\pi A\int dE_1^2\int dE_2^2\int d\theta\, P_1(E_1^2)P_2(E_2^2)P_\theta(\theta) \times \delta(E^2-E_1^2-E_2^2-2E_1E_2\cos\theta). \quad (1)$$

Here, $P_i(E_i^2)$ for $i=1,2$ denotes the probability distribution of the ith signal as a function of E_i^2, normalized by $\int dE_i^2\, P_i(E_i^2)=1$, $P_\theta(\theta)$ is the probability distribution for θ, and A is a normalization constant. The δ function enforces the vector addition.

If the two signals are produced independently in either the same source region or different regions then the angle θ should be uniformly distributed and so $P(\theta)=(2\pi)^{-1}$. This assumption is made henceforth. Performing the θ integral using the δ function involves the standard identity

$$\int dx\ f(x)\delta[G(x)]=\sum_{x_i}\frac{f(x_i)}{|dG/dx|_{x_i}}, \tag{2}$$

where x_i are the roots of $G(x)=0$. For the θ integral, $G(\theta)=E^2-E_1^2-E_2^2-2E_1E_2\cos\theta$, with a root at

$$\cos\theta=(E^2-E_1^2-E_2^2)/2E_1E_2 \tag{3}$$

and

$$\left|\frac{dG}{d\theta}\right|=2E_1E_2|\sin\theta|=\sqrt{|4E_1^2E_2^2-(E^2-E_1^2-E_2^2)^2|}. \tag{4}$$

Rearranging the square root factor in Eq. (4), Eqs. (1)–(4) lead to

$$P(E^2)=A\int dE_1^2 \times\int dE_2^2\frac{P_1(E_1^2)P_2(E_2^2)}{\sqrt{|[E^2-(E_1+E_2)^2][E^2-(E_1-E_2)^2]|}}. \tag{5}$$

The square root factor in Eq. (5) contains integrable singularities. These correspond to $\cos\theta=\pm1$; that is, to the vectors $\mathbf{E}_1$ and $\mathbf{E}_2$ being parallel or antiparallel. The requirement $-1\leqslant\cos\theta\leqslant1$ also constrains the integration domain in E_1-E_2 phase space, as discussed next.

Figure 2 illustrates the singularities and allowed domain of E_1-E_2 phase space for the integration in Eq. (5). First, the factor $E^2-(E_1+E_2)^2$ in Eq. (5) implies singularities along the lines $E=\pm(E_1+E_2)$, of which only the positive solution is physical, corresponding to $\cos\theta=+1$. Second, the factor $E^2-(E_1-E_2)^2=(E-E_1+E_2)(E+E_1-E_2)$ implies singularities along the lines $E_2=E_1-E$ and $E_2=E_1+E$, both of which are physical and correspond to $\cos\theta=-1$. Restricting E, E_1, and E_2 to be positive definite, the physical portions of these three singularity lines are shown in Fig. 2 (solid lines). In comparison, for $\cos\theta=0$, Eq. (3) yields the equation of a circle centered at the origin with radius E (dashed line in Fig. 2): $E^2=E_1^2+E_2^2$. Considering the requirement $|\cos\theta|\leqslant1$ and the above singularities, the allowed domain of integration in Eq. (5) thus lies interior to the three physical singularity lines as shown in Fig. 2.

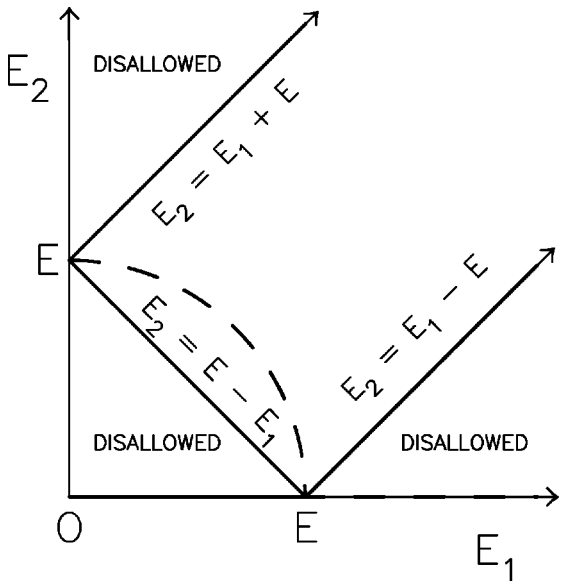

FIG. 2. E_1-E_2 space, the singularities and the allowed domain.

How does the prediction (5) differ from those calculated by assuming simple convolution of the wave intensities or wave amplitudes? Noting that the intensity $I\propto E^2$, intensity convolution corresponds to

$$P_I(E^2)=A\int dE_1^2\int dE_2^2\ P_1(E_1^2)P_2(E_2^2)\,\delta(E^2-E_1^2-E_2^2) \tag{6}$$

$$=A\int dE_1^2\ P_1(E_1^2)P_2(E^2-E_1^2). \tag{7}$$

In comparison, convolution of the wave amplitudes, corresponding to nonvectorial addition of the field magnitudes, leads to

$$P_E(E^2)=A\int dE_1^2\int dE_2^2\ P_1(E_1^2)P_2(E_2^2)\,\delta(E-E_1-E_2) \tag{8}$$

$$=A\int dE_1^2\ 2|E-E_1|P_1(E_1^2)P_2([E-E_1]^2). \tag{9}$$

The absence of singularities in Eqs. (7) and (9) compared with Eq. (5), and the different multiplicative factors and functional dependences of the term $P_2(E_2^2)$ make it clear that intensity convolution and simple field addition, generally, yield different results from the expression (5) for full vectorial convolution. It is, therefore, important to calculate the statistics of combined signals by using the prediction (5).

Explicit expressions for the distributions P_1 and P_2 are required before proceeding to numerical results. A Gaussian distribution $P_G(E^2)$ in E^2 or I is described by

$$P_G(E^2)=(\sqrt{2\pi}\sigma_I B)^{-1}\ e^{-(E^2-E_0^2)^2/2\sigma_I^2}, \tag{10}$$

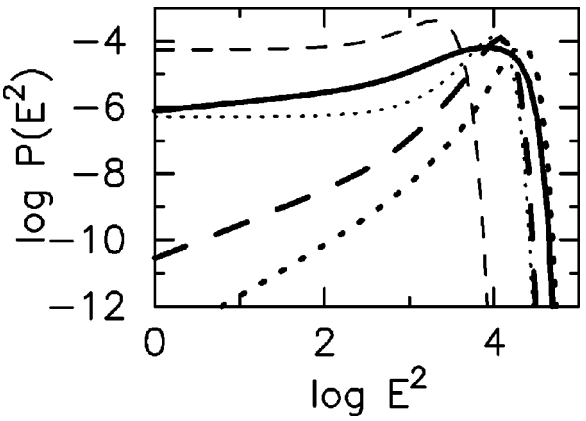

FIG. 3. Probability distribution $P(E^2)$ (thick solid line) for the vectorial convolution (5) of the two Gaussian distributions in Table I. Here and below $\log \equiv \log_{10}$. Thick dashed and dotted lines show the predictions (6) and (7), respectively, for intensity and amplitude convolution. Thin dashed and dotted lines show the two individual distributions.

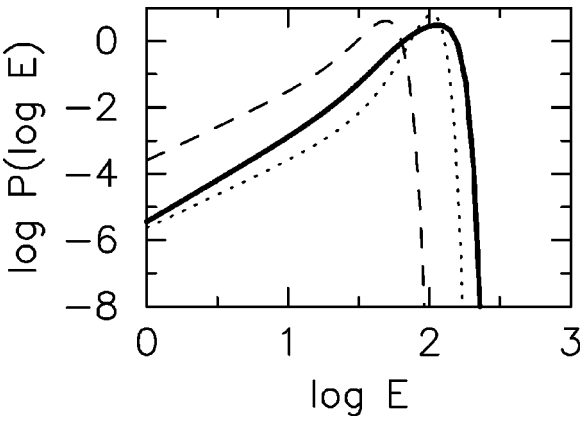

FIG. 4. The distribution $P(\log E) = P(\log_{10} E)$ for the same parameters and using the same line styles as Fig. 3.

where E_0^2 and σ_I are the average and standard deviation of E^2, $2B = 1 + \mathrm{erf}(E_0^2/2\sigma_I)$, and erf represents the usual error function. The expression for a lognormal distribution $P_{LN}(E^2)$ is obtained by converting the definition

$$P_{LN}(\log E) = (\sqrt{2\pi}\sigma)^{-1} e^{-(\log E - \mu)^2/2\sigma^2}, \tag{11}$$

normalized using $\int d(\log E) P_{LN}(\log E) = 1$, where $\log E = \log_{10} E$, to the form for an integral over E^2. The result is

$$P_{LN}(E^2) = P_{LN}(\log E)/(2E^2 \ln 10). \tag{12}$$

III. NUMERICAL ANALYSES

A. General features and trends

Representative results for the distribution $P(E^2)$ that results from combining two Gaussian distributions are displayed in Fig. 3; the Gaussian parameters are listed in Table I. Shown are the initial distributions themselves and predictions (5)–(9) for the full vectorial, intensity, and amplitude convolutions, respectively, of the initial distributions. Several important results are apparent. First, the full vectorial prediction (5) is significantly different from the intensity and amplitude convolutions (6)–(9): while the distribution's shape is qualitatively similar at high E for the three predictions (but differs in magnitude), at low E, the appearance of an almost flat tail in the full distribution (5) points to an important qualitative difference. Second, the tail at low E for Eq. (5) but not Eq. (6) or Eq. (8) is due to the fully vectorial nature of the convolution, as interpreted in detail below, and not due to Gaussian distributions having a similar tail. Third, the prediction (5) differs significantly from the two input distributions. However, the prediction (5) is closely Gaussian at high E above the peak in $P(E^2)$, differing mostly below the peak. Similar comments apply to the combined distribution $P(\log E)$ shown in Fig. 4; note that the E^2 conversion factor in Eq. (12) between $P(E^2)$ and $P(\log E)$ changes the relatively flat tail at low E for $P(E^2)$ (because $P_G(E^2) \approx (\sqrt{2\pi\sigma_I}B)^{-1} e^{-E_0^4/2\sigma_I^2}$ for $E^2 \ll E_0^2$) into an approximate power-law form with $P(\log E) \propto E^2$.

Figure 5 shows typical results for the combination of a lognormal and a Gaussian distribution, whose parameters are specified in Table I. Once again the vectorial prediction (5) differs qualitatively from those for intensity and amplitude convolutions, primarily through the development of a relatively flat tail at low E. The prediction (5) also differs significantly from the component distributions at E smaller than the peak in $P(E^2)$. Note, however, that the fall off at large E above the peak in $P(E^2)$ is closely lognormal; this corresponds to the lognormal profile of the component distribution that dominates at high E.

Figure 6 shows typical results for two lognormal distributions, whose parameters are in Table I. Results in common with those above are: the strong qualitative differences between the prediction (5) and intensity and amplitude convolutions, the development of the enhanced, relatively flat tail at low E for the prediction (5), significant differences between the component distributions and Eq. (5) below the peak in $P(E^2)$, and the fall off above the peak in $P(E^2)$ has

TABLE I. Gaussian and lognormal parameters for Figs. 3–8. Here, $A_i = \langle E_i^2 \rangle$ or $\langle \log_{10} E_i \rangle$ for a Gaussian or lognormal component, respectively, with σ_i the corresponding standard deviation.

Figure	Component 1	Component 2	A_1	σ_1	A_2	σ_2
3,4	Gaussian	Gaussian	2000	1000	10000	3000
5	Gaussian	lognormal	2000	1000	2.1	0.1
6,7	lognormal	lognormal	1.2	0.2	2.1	0.1
8	lognormal	lognormal	1.2–2.4	0.2	2.1	0.1

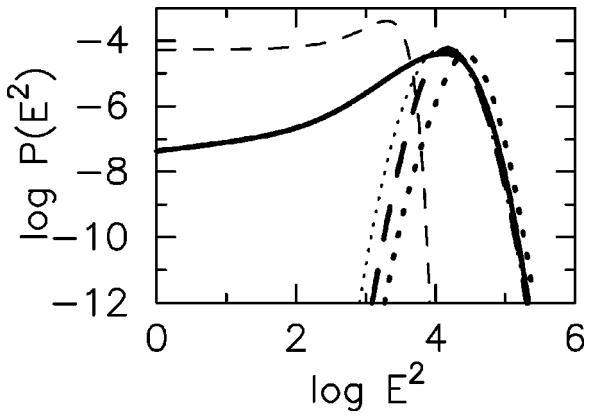

FIG. 5. In the same format as in Fig. 3, the combined distribution $P(E^2)$ for the Gaussian and lognormal components described in Table I.

the same (lognormal) character as the component distribution dominant at high E and the predictions (6) and (7). Figure 7 displays $P(\log E)$ for completeness.

An explanation is needed for the enhanced tail at low E for prediction (5) in Figs. 3–7. This tail is primarily due to the vectorial nature of the convolution for two reasons. First, allowing nonaligned vectors in the vectorial convolution is the primary difference between (5) and predictions (6) and (8). Second, varying the nature and parameters of the component wave distributions does not affect the tail's existence and qualitative behavior but only its height. Consider the case when $\mathbf{E}_1$ and $\mathbf{E}_2$ are antiparallel and have very similar magnitudes, so that $\mathbf{E}=\mathbf{E}_1+\mathbf{E}_2\approx\mathbf{0}$. This case is included in Eq. (5) but not in Eqs. (6) and (7), and clearly leads to a significant contribution to $P(E^2)$ at low E. Specifically, Eq. (5) has an integrable singularity for $E-(E_1-E_2)\approx 0$ corresponding to $\cos\theta=-1$. Thus, physically, the tail at small E for the prediction (5) corresponds to contributions with $\mathbf{E}_1 \approx -\mathbf{E}_2$. This implies that the tail will have a larger magnitude when the two individual distributions have significant overlap and will decrease as the overlap decreases and one individual distribution dominates the other (e.g., $|\mathbf{E}_1| \gg |\mathbf{E}_2|$). Figure 8 confirms this prediction for the case of two

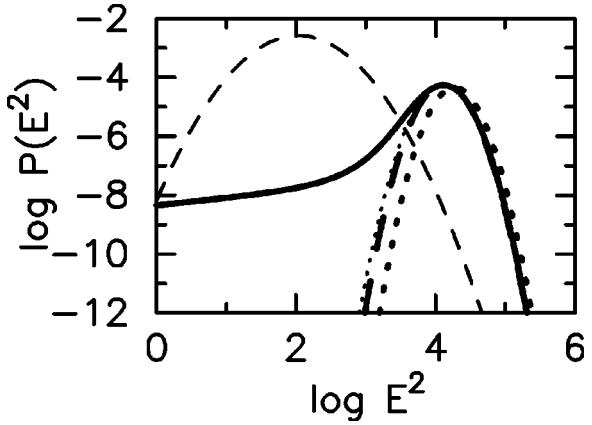

FIG. 6. The combined distribution $P(E^2)$ for the two lognormals described in Table I, displayed in format of Fig. 3.

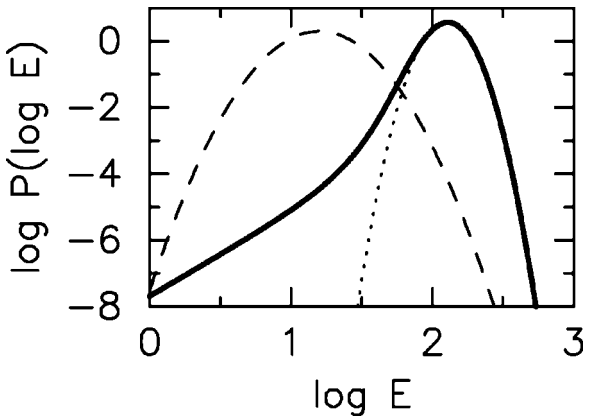

FIG. 7. The combined distribution $P(\log E)$ corresponding to Fig. 6, presented in format of Fig. 4.

lognormals: varying only the parameter μ_1 of one-wave population to change the overlap of the two distributions, the tail height increases strongly as the overlap (and μ_1) increases before peaking and then decreasing again as μ_1 exceeds μ_2. Figure 8 also shows that the combined distribution (5) can have an approximate power-law form at high E (e.g., the dotted and dash-dot curves) as discussed more in Sec. III B.

These and analogous figures demonstrate that the full vectorial convolution (5) differs markedly from the simpler intensity and amplitude convolution results (6) and (8), principally through the enhanced tail at low E. Another general result is that at large E, near and above the peak in the combined $P(E^2)$ distribution, predictions (5)–(9) differ quantitatively but fall off very similarly to the dominant individual distribution, defined as the distribution either centered at or extending further to higher E. While amplitude or intensity convolution is a reasonable approximation to the result (5) near and above the peak in $P(E^2)$, it clearly fails at low E. Accordingly, the full vectorial result (5) should be used in general.

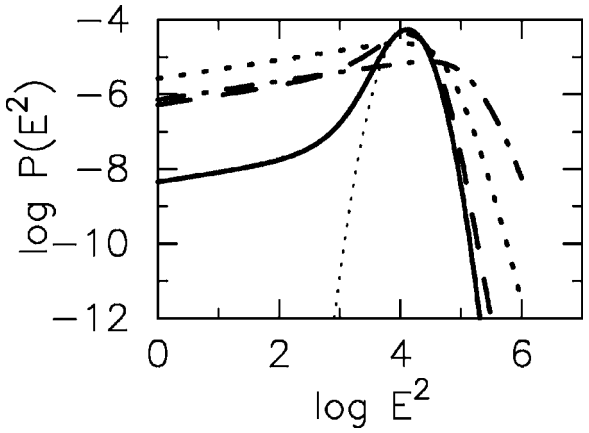

FIG. 8. Evolution of the combined distribution $P(E)^2$ (thick lines) given by Eq. (5) as a function of the overlap between two contributing lognormals. Holding the second lognormal constant ($\mu_2=2.1$ and $\sigma_2=0.1$—thin dotted line), the centroid μ_1 of the first lognormal is 1.2 (solid), 1.6 (dashed), 2.0 (dotted), and 2.4 (dash-dot) for constant $\sigma_1=0.1$. Here $\log\equiv\log_{10}$.

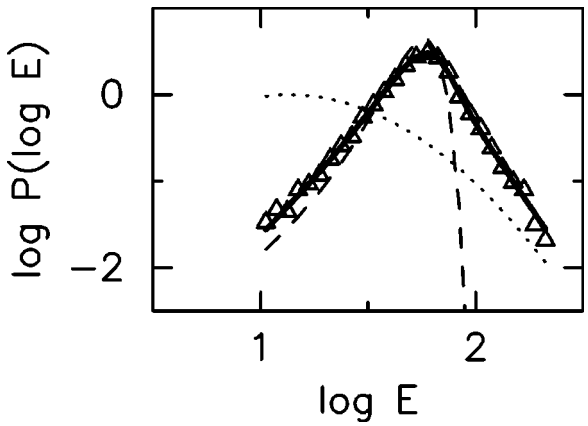

FIG. 9. The observed distribution $P(\log E)$ for Vela at phase 450 (triangle symbols) is compared with the best fit (thick solid line) to the prediction (5) for the combination of a Gaussian and a lognormal component (thin dashed and dotted lines, respectively). Here $\log \equiv \log_{10}$. The fitting procedure and fit parameters are described in the text.

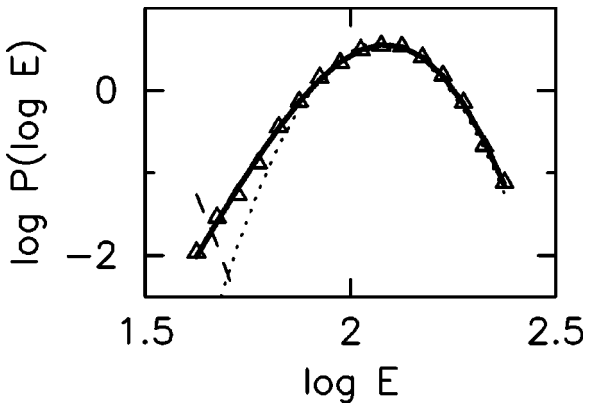

FIG. 10. Vela data (triangle symbols) and theoretical fits to Eq. (5) for the distribution $P(\log E)$ at phase 510, with $\log \equiv \log_{10}$. Thick solid and dashed lines show best fits for the double-lognormal and Gaussian-lognormal combinations, respectively, while thin dashed and dotted lines show the individual distributions for the best-fit double-lognormal combination.

B. Development of domains with apparent power-law character

Domains in which the distributions $P(E^2)$ and $P(\log E)$ appear to vary with a power-law form are important both theoretically and observationally, particularly in connection with the SOC and interpretations of observational data. It has already been shown that an approximate E^2 form is typical for the $P(\log E)$ distribution at low E due to the slowly varying tail at low E for the $P(E^2)$ distribution (5). The purpose of this section is to show that combining a lognormal distribution with either a lognormal or Gaussian distribution can also lead to the combined distribution (5) having a closely power-law form in a restricted domain at high E. Since the asymptotic form at high enough E is still imposed by the individual distribution which extends to higher E (see Figs. 3–8), these power-law regions occur at intermediate E, near where the curves $P(E^2)$ cross for the individual distributions and a transition exists between which individual distribution dominates at higher E.

These power-law domains at high E typically develop as follows: a lognormal distribution is centered at low E but has large enough σ such that it extends to larger E than the second, more intense, but narrower wave distribution, which may be either Gaussian or lognormal. Then, at high enough E, the combined distribution (5) changes its functional form from the one determined by the second distribution towards that for the underlying high σ lognormal, often leading to a domain, in which the combined distribution appears power law. Note, moreover, that the lognormal distribution shows an approximately linear slope in log-log plots for $\log E \gg \mu$, thereby appearing as a local power law. This is illustrated in Fig. 8 for the combination of two lognormals (e.g., see the dotted and dash-dot curves) and in Fig. 9 below for the lognormal-Gaussian combination.

Thus, as discussed in more detail below, the appearance of approximately power-law statistics does not necessarily mean that an interpretation in terms of an intrinsic power-law distribution (and SOC) is in order. Instead, the statistics may be due to the combination of two underlying wave distributions, at least one of which is lognormal with a large enough σ to dominate the other at large enough E. It may not be possible to reliably distinguish between these possibilities unless the domain in $\log E$ (and the number of counts in the entire distribution) is large enough, ideally at least a decade in $\log E$.

IV. APPLICATION TO THE VELA PULSAR

Radio emissions from pulsars are well known to vary greatly in intensity, sometimes by more than an order of magnitude, both from pulse to pulse at a given phase and also between neighboring phases (time samples) within a pulse despite each pulsar having a very well-defined pulse profile when averaged over thousands of pulses [30]. Recently, a dataset of about 20 000 contiguous, rapidly sampled, and coherently dedispersed pulses was obtained for the Vela pulsar [28,29]. The intensity was sampled 2048 times per pulse, or about every 44 μs, corresponding to 2048 ''phase'' bins for the pulsar's rotation. First analyses of these data at a number of pulse phases [26] provide strong evidence that the field statistics are lognormal, supporting the interpretation that pure SGT is relevant and strongly constraining the emission mechanism and physics of the source. However, at other pulse phases the observed field statistics either are not well fitted by a single lognormal component or appear approximately power-law at high fields above a Gaussian noise background. Here, the formalism and results of Secs. II and III are applied to the Vela dataset, resulting in greatly improved fitting and understanding of the observed field statistics and showing that the high-E power law is best interpreted in terms of vector convolution of a Gaussian background component with an emerging lognormal component (cf. Sec. III B). In addition, results at other phases are best interpreted in terms of the combination of two underlying lognormal distributions. A detailed analysis of these data with vectorially combined two-component fits for a wide range of pulsar phases is underway [31,32].

Figure 9 shows the $P(\log E)$ distribution observed for

phase 450 (triangle symbols), a phase at which the pulsar is above background but before the peak in the average profile. This distribution is obtained by binning the time series of data for this phase in $\log E$ and normalizing. Here, E is defined by $E^2=I$ in terms of the intensity I (actually the flux density, which equals the intensity divided by the detector's 20 MHz bandwidth), measured in millijanskys (mJy) with 1 mJy$=10^{-29}$ W m^{-2} Hz^{-1}. In Fig. 9, note the approximately power-law variations, both above and below the peak. The thick solid line shows the result of fitting (5) for the combination of one Gaussian and one lognormal distribution, obtained by minimizing χ^2 using the amoeba routine [33]. The best-fit parameters are $I_0=E_0^2=2900$ mJy and $\sigma_I=1300$ mJy for the Gaussian, cf. Eq. (10), and $\mu=1.13$ and $\sigma=0.40$ for the lognormal, cf. Eq. (11). This fit agrees well with the data and has good statistical significance: $\chi^2=33.9$ with 26 bins, yielding a significance probability $P=0.14$. The fitted component distributions are shown with dashed and dotted lines. In comparison, single-component Gaussian or lognormal fits clearly fail and have poor statistical significance ($\chi^2 \gtrsim 10^3$ and $P<10^{-20}$). Double-lognormal fits are similarly poor for these data.

Analyses at other phases (not shown here [31,32]) clearly demonstrate that the lognormal component evolves significantly as a function of phase while the Gaussian component corresponds primarily to the Gaussian field statistics observed off pulse, where measurement noise and sky background dominate. This figure is thus important for two reasons. First, it demonstrates that these pulsar data are well fitted by the combination of a Gaussian (noise) component and an emerging lognormal component (which dominates increasingly in the phase range 460–540). Second, it provides an explicit experimental demonstration that apparently power-law probability distributions can be due to vectorial convolution of two underlying component distributions, neither of which have power-law statistics. Care must, therefore, be taken in interpreting apparently power-law statistics.

Figure 10 addresses Vela data for phase 510, which appear strongly lognormal. The best fit to Eq. (5) for two lognormal component distributions (thick solid line) has $\mu_1=2.2$, $\sigma_1=0.10$, $\mu_2=1.3$, and $\sigma_2=0.11$ in Eq. (11). It agrees very well with the data and has good statistical significance: $\chi^2=21.1$ for 15 bins, yielding $P=0.14$. The corresponding Gaussian-lognormal fit has $\chi^2=1551$ and minimal statistical significance (thick dashed line). Thin dashed and dotted lines delineate the underlying component distributions for the double-lognormal combination, with one being located at small $\log E \lesssim 1.8$. The fits for the double-lognormal and Gaussian-lognormal differ primarily in the tail at low $\log E \lesssim 1.8$, with the Gaussian-lognormal combination significantly overpredicting the tail's level. Accordingly, the combined distribution (5) can be used to discriminate between the form of the underlying distributions even when one distribution is primarily localized at much lower fields than the other.

V. DISCUSSION OF THE VELA DATA

The foregoing analyses show that Vela's variability is well modeled in terms of a lognormal component that dominates at high E and is the dominant contributor to the pulsar's emission, superposed with either a Gaussian or a second lognormal component at low E. Lognormal statistics are consistent with SGT and inconsistent with, first, the power-law statistics expected for SOC or nonlinear self-focusing instabilities, or driven thermal waves [5,6,21,13,15] and, second, the flat $P(\log E)$ distribution expected for uniform secular growth [8]. This means that Vela's field statistics are consistent with the source plasma being in an SGT state [26]: the pulsar's emission corresponds to a plasma instability operating stochastically near marginal stability, with self-consistent wave-particle interactions occurring in a plasma with independently prescribed inhomogeneities. The source is not in an SOC state.

The radio emission mechanism is also strongly constrained by the observed statistics. The absence of intrinsic power-law statistics at high E for these phases is inconsistent with nonlinear self-focusing instabilities being important, contrary to several previous suggestions [34–36]. Similarly, the absence of a cutoff in the lognormal distributions at high E is inconsistent with a nonlinear decay process being important. Thus, these data are consistent with the Vela pulsar's emission mechanism being linear [26], either generating radiation directly by a linear instability in an SGT state or indirectly via linear mode conversion of nonescaping waves driven by a linear instability in an SGT state. These analyses and associated theoretical interpretations provide strong evidence that pulsar radiation is often generated by linear processes, complementing recent purely theoretical arguments [37,38].

The origin of the second lognormal component has not been addressed before. The simplest possibility is that it is a second, weaker, emission produced in an SGT system located in either the same or, more probably, a different source region. Evolution of the second component from Gaussian intensity statistics to lognormal statistics (and then back) across the source is then interesting. If the Gaussian component were solely instrumental noise then it should be present and unchanging at all phases. Since scattering can lead to Gaussian intensity statistics [1], these changes in the Gaussian component at some phases may be interpretable, somewhat speculatively, in terms of scattering and propagation effects acting on an intrinsically lognormal component, with the lognormal component escaping with minimal scattering at other phases. Further work is required to test this interpretation.

Before proceeding to discuss other applications of the formalism, it is cautioned that pulsar emission mechanisms may potentially vary from phase to phase and from pulsar to pulsar. This is evidenced by observations of power-law field statistics for so-called giant pulses from the Crab pulsar and some millisecond pulsars [39–41], as well as for so-called giant micropulses from phases 430 to 434, only, for the Vela pulsar [28,29]. The indices observed for these $P(E)$ distributions, ranging from ≈ -4 to -7, are not inconsistent with those expected [12,13] for the nonlinear self-focusing process of wave collapse [32]. These variations emphasize the importance of field statistics for understanding remote space and astrophysical sources.

The formalism developed in this paper should be immediately applicable to other pulsars, as well as to other radio emissions from solar system and other astrophysical sources. Possible candidates include Jovian ''*S*'' bursts [22], solar radio bursts, and astrophysical masers. The formalism, perhaps adapted to consider signal detection with a one-dimensional rotating spacecraft antenna, also is relevant to superposition of plasma waves. Known examples of such superpositions are currently treated by restricting analysis to high E well above the background (where the form of the combined distribution agrees closely with the dominant component per Sec. III's analyses) or else assuming a δ function in E for the second component. They include: (1) the near-Earth solar wind and edge of Earth's foreshock, where radio waves just above f_p occur with thermal Langmuir waves and driven thermal Langmuir waves, respectively [15], (2) waves near f_p occur with whistler-mode hiss below f_p over Earth's polar cap [25], and (3) bursty Langmuir waves occur with whistler-mode hiss at auroral latitudes in and above Earth's ionosphere [42].

VI. CONCLUSIONS

Statistics of wave fields can be used to constrain the physics of the emission mechanism and source region [6–12,14,15,17–20,23–27,31,32]. Superposition of waves generated by several mechanisms or in several sources can make it difficult to interpret the statistics. Accordingly, an analytic expression for the field statistics resulting from vector superposition of two-component field distributions has been derived and the resulting two-dimensional integral solved numerically. This probability distribution for two vectorially combined fields differs, in general, from both the component distributions and the distributions resulting from amplitude or intensity convolution. It typically follows the qualitative form of the dominant individual component at high E, but not at fields below the peak, where a significant tail develops. This low-E tail has no counterpart in the predictions for amplitude or intensity convolution, instead resulting from vector convolution of approximately antiparallel vectors of similar magnitude from the two-component distributions. It is most prominent when the two individual distributions overlap substantially.

Approximately power-law distributions can develop at high E from vector convolution of a lognormal with either a lognormal or Gaussian, with neither individual distribution being power law. At low E below the peak, a power law develops in the combined $P(\log E)$ distribution when the tail is approximately flat in the $P(E^2)$ distribution, corresponding to individual components having substantial overlap at high E, both for lognormal-lognormal and Gaussian-lognormal combinations. At intermediate but high E a power-law tail can develop in a restricted domain of E, near where a lognormal centered at low E, but with large variance σ^2, eventually dominates a second, narrower distribution centered at higher E than the first. Similarly, at high E, a lognormal distribution may appear power law over a limited range of E. Care must, thus, be taken in interpreting approximate power-law distributions in terms of SOC, SGT, and/or vectorial combinations of signals without intrinsic power-law distributions.

These predictions are illustrated using recent data from the Vela pulsar, with major implications for pulsar physics. They are found to fit well, both quantitatively and with high statistical significance, with Gaussian-lognormal and double-lognormal combinations applying in different phase domains that cover most of Vela's pulse profile. The Gaussian-lognormal fits are appropriate at phases where the observed distributions $P(\log E)$ and $P(E^2)$ have nearly power-law domains at large E: these power laws are thus not intrinsic but correspond to vector convolution of two non-power-law distributions. These data are best interpreted in terms of the pulsar's emissions having lognormal statistics at these phases. This is strong evidence that the emissions are generated in an SGT system, corresponding to a plasma instability operating near marginal stability in an inhomogeneous plasma. Moreover, the absence of intrinsic power-law statistics or cutoffs in these distributions is consistent with the radiation being generated by a purely linear instability, either directly or else indirectly via linear mode conversion of nonescaping waves produced by an instability, and inconsistent with SOC or nonlinear self-focusing mechanisms proposed previously. The utility and power of field statistical techniques, as well as the richness of pulsar physics, is emphasized by pointing out that giant pulses from other pulsars and giant micropulses from Vela (in a distinct, very localized, range of phases from those analyzed here) have power-law statistics with indices not inconsistent with nonlinear self-focusing instabilities. Finally, the theoretical predictions presented and illustrated here are expected to be widely applicable to plasma waves and radiation propagating from space and astrophysical sources or observed in laboratory and space plasmas. More generally, this research is relevant to the analysis and interpretation of field statistics for waves growing in inhomogeneous media, such as optical fibres and other materials with randomly embedded lasers, and perhaps ocean acoustics.

ACKNOWLEDGMENTS

The Australian Research Council funded this work. We thank S. Johnston for access to the Vela data and helpful discussions.

[1] B.J. Rickett, Annu. Rev. Astron. Astrophys. **28**, 561 (1990).
[2] N.A. Krall and A.W. Trivelpiece, *Principles of Plasma Physics* (McGraw-Hill, New York, 1973).
[3] D.B. Melrose, *Instabilities in Space and Laboratory Plasmas* (Cambridge University Press, Cambridge, UK, 1986).
[4] T.H. Stix, *Waves in Plasmas* (AIP, New York, 1992).

[5] P. Bak, C. Tang, and K. Wiesenfeld, Phys. Rev. Lett. **59**, 381 (1987)
[6] P. Bak, *How Nature Works* (Copernicus, New York, 1996).
[7] P.A. Robinson, Sol. Phys. **139**, 147 (1992).
[8] P.A. Robinson, I.H. Cairns, and D.A. Gurnett, Astrophys. J. **407**, 790 (1993).
[9] I.H. Cairns and P.A. Robinson, Geophys. Res. Lett. **24**, 369 (1997).
[10] I.H. Cairns and P.A. Robinson, Phys. Rev. Lett. **82**, 3066 (1999).
[11] P.A. Robinson and I.H. Cairns, Phys. Plasmas **8**, 2394 (2001).
[12] P.A. Robinson and D.L. Newman, Phys. Fluids B **2**, 2999 (1990).
[13] P.A. Robinson, Rev. Mod. Phys. **69**, 507 (1997).
[14] P.A. Robinson, Phys. Plasmas **2**, 1466 (1995).
[15] I.H. Cairns, P.A. Robinson, and R.R. Anderson, Geophys. Res. Lett. **27**, 61 (2000).
[16] D.B. Melrose and G.A. Dulk, Astrophys. J. **259**, 844 (1982).
[17] P.A. Robinson, H.B. Smith, and R.M. Winglee, Phys. Rev. Lett. **76**, 3558 (1996).
[18] J.M. Carlson and J.S. Langer, Phys. Rev. Lett. **62**, 2632 (1989).
[19] J.J. Binney, N.J. Dowrick, A.J. Fisher, and M.E.J. Newman, *The Theory of Critical Phenomena* (Oxford University Press, Oxford, UK, 1992).
[20] E.T. Lu and R.J. Hamilton, Astrophys. J. **380**, L89 (1991).
[21] M.D.T. Young and B.G. Kenny, Astron. Soc. Pac. Conf. Ser. **105**, 179 (1996).
[22] J. Queinnec and P. Zarka, Planet. Space Sci. **49**, 365 (2001).
[23] C. Boshuizen, I.H. Cairns, and P.A. Robinson, Geophys. Res. Lett. **28**, 3569 (2001).
[24] I.H. Cairns and K.A. Grubits, Phys. Rev. E **64**, 056408 (2001).
[25] I.H. Cairns and J.D. Menietti, J. Geophys. Res., [Space Phys.] **106**, 29 515 (2001).
[26] I.H. Cairns, S. Johnston, and P. Das, Astrophys. J. **563**, L68 (2001).
[27] H. Isliker and A.O. Benz, Astrophys. J. **375**, 1040 (2001).
[28] S. Johnston, W. van Straten, M. Kramer, and M. Bailes, Astrophys. J. **549**, L101 (2001).
[29] M. Kramer, S. Johnston, and W. van Straten, Mon. Not. R. Astron. Soc. **334**, 523 (2002).
[30] R.N. Manchester and J.H. Taylor, *Pulsars* (Freeman, San Francisco, 1977).
[31] I.H. Cairns, P. Das, and S. Johnston (unpublished).
[32] I.H. Cairns, P. Das, P.A. Robinson (unpublished).
[33] W.H. Press, B.P. Flannery, S.A. Teukolsky, and W.T. Vetterling, *Numerical Recipes* (Cambridge University Press, New York, 1986).
[34] E. Asseo, G. Pelletier, and H. Sol, Mon. Not. R. Astron. Soc. **247**, 529 (1990).
[35] E. Asseo, Astron. Soc. Pac. Conf. Ser. **105**, 147 (1996).
[36] J.C. Weatherall, Astrophys. J. **506**, 341 (1998).
[37] D.B. Melrose, Astron. Soc. Pac. Conf. Ser. **105**, 139 (1996).
[38] M.E. Gedalin, E. Gruman, and D.B. Melrose, Phys. Rev. Lett. **88**, 121101 (2002).
[39] S.C. Lundgren, J.M. Cordes, M. Ulmer, S.M. Matz, S. Lomatch, R.S. Foster, and T. Hankins, Astrophys. J. **453**, 433 (1995).
[40] I. Cognard, J.A. Shrauner, J.H. Taylor, and S.E. Thorsett, Astrophys. J. **457**, L81 (1996).
[41] S. Johnston and R. Romani, Mon. Not. R. Astron. Soc. **332**, 109 (2002).
[42] K.L. McAdams, J. Labelle, M.L. Trimpi, P.M. Kintner, and R.A. Arnoldy, J. Geophys. Res., [Space Phys.] **104**, 28109 (1999).